Comparative analysis of pattern reconstruction using orthogonal moments

Alfonso Padilla-Vivanco, MEMBER SPIE
Universidad Politécnica de Tulancingo
División de Ingenierías
Prolongación Guerrero No. 808
Tulancingo, Hidalgo, México
E-mail: apadilla@inaoep.mx

Gonzalo Urcid-Serrano, MEMBER SPIE
Fermín Granados-Agustín, MEMBER SPIE
Alejandro Cornejo-Rodríguez
Instituto Nacional de Astrofísica
Óptica y Electrónica Apartado Postal 51 y 216
C. P. 72000
Tonantzintla, Puebla, México

Abstract. We present a detailed analysis of the reconstruction of gray-level images using orthogonal moments with respect to the basis sets of Zernike, Fourier-Mellin, Chebyshev-Fourier, and pseudo-Jacobi-Fourier polynomials. As test images, we use Ronchigrams with different numbers of fringes as high-spatial-frequency components. The evaluation of image reconstruction between orthogonal moment sets is made in terms of different metrics. These measurements are the normalized image reconstruction error, the overall activity level in each image with respect to spatial frequency variations, the root-mean-square contrast, the total number of reconstructed fringes, the coordinate transformations of the input image, and the number of moment orders. Moreover, a method of denoising the input image based on the Daubechies wavelet transform is implemented to compute the signal-to-noise ratio. Numerical computations show that, for the Ronchigram reconstructions, the performance of Zernike moments is better than that of the other basis sets of orthogonal moments.
© 2007 Society of Photo-Optical Instrumentation Engineers. [DOI: 10.1117/1.2432878]

Subject terms: orthogonal moments; image reconstruction; circular complex polynomials; grey-level images; Ronchigrams; interference patterns.

Paper 060171R received Mar. 9, 2006; revised manuscript received Jun. 25, 2006; accepted for publication Jun. 28, 2006; published online Jan. 26, 2007. This paper is a revision of a paper presented at the SPIE conference on Optics in Atmospheric Propagation and Adaptive Systems VI, Barcelona, Spain, Sep. 2003. The paper presented there appears (unrefereed) in SPIE proceedings Vol. 5237.

1 Introduction

Moments have played an important role in pattern recognition, image analysis, and machine vision applications in the last years.[1–4] In 1961, Hu[5] used geometric moments to generate a set of invariants; however, the recovery of the image from these kinds of moments has been found to be quite difficult, since they do not have the orthogonality property. Two decades after Hu, in 1980, Teague[6] proposed Zernike moments derived from the basis set of orthogonal Zernike polynomials. Zernike moments have been shown to be rotation-invariant and robust to noise. Also, a relatively small set of Zernike moments can characterize effectively the global shape of a pattern.

Other orthogonal moments are derived from the Legendre, Chebyshev, orthogonal Fourier-Mellin,[7] Chebyshev-Fourier,[8] and pseudo-Zernike polynomials.[9] In general, low-order moments represent the global shape of an image, and high-order moments the detail. Specifically, image reconstruction using orthogonal Fourier-Mellin moments (OFMMs) and Chebyshev-Fourier moments (CHFMs) have shown almost the same results and are superior to other moment sets in describing binary images.[8] Recently, a new set of orthogonal moments has been proposed, based on the pseudo-Jacobi-Fourier[10] polynomials. As stated by Amu et al.[10] the pseudo-Jacobi radial polynomials of order n have almost $n+2$ uniformly distributed

zeros within the radial distance interval $0 \leq r \leq 1$. This means that these moments can describe with very good accuracy the high-spatial-frequency components, as has recently been proven using practical binary images.[10] However, for the case of images in grayscale with some kind of simple geometric structure, such as interferograms or Ronchigrams,[11] high- and low-spatial-frequency components correspond, respectively, to sharp and smooth transitions of gray-level intensities. These intensity transitions can be difficult to retrieve by means of certain kinds of moments.

In the recent literature there have been analyzed several orthogonal moment sets for the reconstruction of binary objects, such as ideograms, characters, and digits, that are commonly used as test images in the pattern recognition areas. A lot of the image image analysis has been done with this kind of objects. In this paper we analyze the reconstruction performance of four of the most important sets of circular complex orthogonal moments, using as test images Ronchigrams in gray level, which have a simple geometric structure. This study can be extended to other kinds of scenes also useful in computer vision: interference patterns, diffraction distributions, phase objects, interferograms, etc. The common characteristics of all these scenes are that they present homogeneous regions in gray level with different contrasts against a dark background. From the point of view of the numerical effort, binary and grayscale images require different numbers of moments for their reconstruction: a few low orders are usually enough for the retrieval

Table 1 Radial polynomials: Zernike $R_{nl}(r)$, Mellin $Q_n(r)$, shifted Chebyshev $C_n(r)$, and pseudo-Jacobi $J_n(r)$. Here κ_n and α_n are normalization factors.

Radial polynomial	Radial series expansion	Orthogonality	α_n	κ_n
Zernike $R_{nl}(r)$, $n-\lvert l \rvert$ even, $\lvert n \rvert \le l$	$\sum_{s=0}^{n-\lvert l \rvert/2} \dfrac{(-1)^s(n-s)!}{s!\left(\dfrac{n+\lvert l \rvert}{2}-s\right)!\left(\dfrac{n-\lvert l \rvert}{2}-s\right)!} r^{n-2s}$	$\int_0^1 R_{nl}(r)R_{ml}(r)r\,dr=\alpha_n\delta_{mn}$	$\dfrac{1}{2(n+1)}$	$\dfrac{n+1}{\pi}$
Mellin $Q_n(r)$	$\sum_{s=0}^{n}\dfrac{(-1)^{n+s}(n+s+1)!}{(n-s)!s!(s+1)!}r^s$	$\int_0^1 Q_n(r)Q_k(r)r\,dr=\alpha_n\delta_{nk}$	$\dfrac{1}{2(n+1)}$	$\dfrac{n+1}{\pi}$
Chebyshev $C_n(r)$	$\left(\dfrac{1-r}{r}\right)^{1/4}\sum_{s=0}^{\lfloor n+2/2 \rfloor}\dfrac{(-1)^s(n-s)!}{s!(n-2s)!}[2(2r-1)]^{n-2s}$	$\int_0^1 C_n(r)C_k(r)r\,dr=\alpha_n\delta_{nk}$	$\dfrac{\pi}{8}$	$\dfrac{8}{\pi}$
Pseudo-Jacobi $J_n(r)$	$(-1)^n\left[\dfrac{2n+4}{(n+3)(n+1)}(1-r)r\right]^{1/2}\sum_{s=0}^{n}\dfrac{(-1)^s(n+s+3)!}{(n-s)!s!(s+2)!}r^s$	$\int_0^1 J_n(r)J_k(r)r\,dr=\alpha_n\delta_{nk}$	1	$\dfrac{1}{2\pi}$

of binary images, whereas high-order moments play a more important role in the reconstruction of gray-level images. Particularly, in Ronchigram analysis the detail of fringes is important to evaluate transverse optical aberrations; a change of spatial frequency is commonly used to increase the accuracy of evaluation.

On the other hand, inside the unit circle there exists an infinite number of orthogonal sets of polynomials; this fact was shown by Bathia and Wolf.[12] Similar to the OFMM,[7] the CHFM and the *pseudo-Jacobi-Fourier moment* (PJFM) correspond to a single set of orthogonal radial polynomials for all circular harmonic orders, contrary to the Zernike moments, which correspond to several orthogonal radial polynomials, one for every harmonic order. In this work, we compare the image reconstruction performance using the Zernike, Fourier-Mellin, Chebyshev-Fourier, and pseudo-Jacobi-Fourier moments. We show that the Zernike moments give the best performance for the retrieval of grayscale images with the kind of geometric structure illustrated in the Ronchigrams used in this research as test images. We compute the orthogonal moments of Ronchigrams by means of two transformations in the image coordinate plane: the first when the image is mapped inside the unit circle, and the second when it is mapped outside.[13,14]

It is well known that experimental images suffer from noise, which is inevitably taken up by the acquisition system. This problem affects the image reconstruction mainly in the higher orders, so that as a partial solution, the denoising of the input image is implemented. Here a simple solution for removing noise is offered by wavelet transformation of the input image and followed by application of a coefficient elimination rule. Alternatively, other noise removal methods like the median or Gaussian filter can be used,[15–17] but the wavelet transformation is particularly effective and easy to use in this context. Additionally, it is a common task to handle additive noise when the images are acquired under incoherent illumination. In the case of coherent optical imaging, multiplicative noise like speckle appears very frequently. In this research the test images have been acquired with a white light source as illuminator. As a consequence, additive noise is assumed in the denoising process of images.

The applications of the pattern reconstruction have already been implemented for deblurring and enhancement of point spread functions (PSFs). Visual improvement by deblurring the PSF using Zernike moments and its reconstruction has been shown in 3-D images of confocal microscopes.[18]

Other possible choices of polynomial bases to reconstruct images are the scaled Chebyshev and Krawtchouk moments.[19,20] These kinds of polynomials have the advantage that no discrete approximation is required in their numerical implementation, and also they are suitable for data stored in rectangular pixel grids as images. However, the feature descriptors that are invariant with respect to rotations in the image plane have to be found using radial-polar moments, such as Zernike moments. Additionally, Chebyshev and Krawtchouk moments are not defined with respect to basis functions of two variables; in some applications such a representation is a disadvantage, as in the characterization and evaluation of visual information that is presented in an optical system. Whereas only the low orders of Zernike moments offer a representation of the aberrations of the optical systems, these orders are needed in applications such as adaptive optics or 3-D fluorescence microscopy.[21]

Our exposition is organized as follows: in Sec. 2 is presented a general review of the orthogonal moments of an image, based on complex circular polynomials. This review includes orthogonality properties of the polynomial sets used. In Sec. 3, the discrete version of the moments and the reconstruction of Ronchigrams with different numbers of fringes are presented. The grayscale image reconstructions are evaluated with the normalized image reconstruction error (NIRE). Other image quality metrics used to measure the results are also described. Section 4 presents a brief
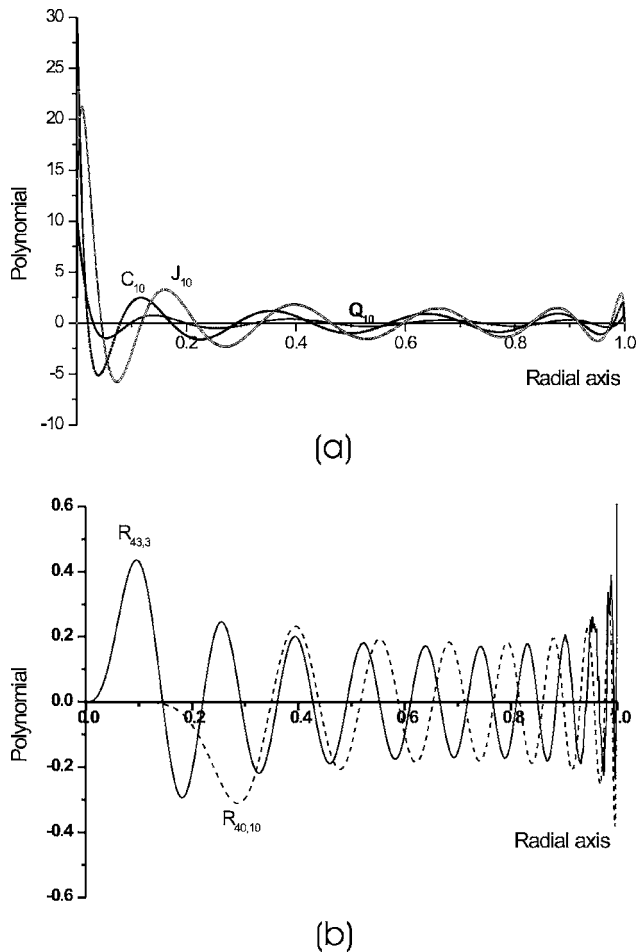
Fig. 1 Radial polynomials. (a) For the order $n=10$, $C_{10}(r)$, $Q_{10}(r)$, and $J_{10}(r)$ are already confined to the interval $(-10,30)$. (b) Zernike polynomials of all orders are confined to the interval $(-1,1)$.

review of the geometric moments needed to compute the digital radius of an object with circular symmetry. A noise removal method by means of wavelet transforms is presented in Sec. 5. The objective is to reduce the NIRE by means of noise filtering of the input image. Finally, in Sec. 6, the conclusions of our research are presented.

2 Review of Orthogonal Moments

As we pointed out in the Introduction, there are an infinite number of complete polynomial sets that are orthogonal inside the unit circle. These polynomial sets provide rotation-invariant moments of a function. A general expression for the orthogonal moments A_{nl} of order n and repetition l for a given function $f(r,\theta)$ in polar coordinates is

$$A_{nl} = \kappa_n \int_0^{2\pi} \int_0^1 f(r,\theta) p_{nl}^*(r,\theta) r \, dr \, d\theta, \qquad (1)$$

where κ_n is a normalization factor, and the complex functions given by

Table 2 In the Zernike expansion $m_Z=0,2,4,6,\dots$ produce respectively 1,6,15,28,… terms. With the others sets, $m_g=0,1,2,3,\dots$ produce the same number of terms 1,6,15,28,…. So $m_Z=2m_g$.

	Number of real expansion terms	
Order $n=l=m$	Zernike	Mellin-Fourier, Chebyshev-Fourier, pseudo-Jacobi-Fourier
0	1	1
1	3	6
2	6	15
3	10	28
4	15	45
5	21	66
6	28	91

$$p_{nl}(r,\theta) = \begin{Bmatrix} R_{nl}(r) \\ g_n(r) \end{Bmatrix} e^{il\theta} \qquad (2)$$

have radial polynomials $R_{nl}(r)$ or $g_n(r)$ in r of degree n. The integers $n \geq 0$ and $l=0,\pm1,\pm2,\pm3,\dots$ are, respectively, the radial and the harmonic orders. If the difference $n-|l|$ is an even number for $|l| \leq n$, the radial Zernike polynomials $R_{nl}(r)$ are used in Eq. (2). Otherwise—if no restriction exists for orders n and l—the polynomials $g_n(r)$ are used. Here, the functions $g_n(r)$ represent the orthogonal Mellin $[Q_n(r)]$, shifted Chebyshev $[C_n(r)]$, or pseudo-Jacobi $[J_n(r)]$ radial polynomials. The series expansions and the orthogonality properties of the radial polynomial sets are given in Table 1.

In general, the zeros of the radial polynomials $g_n(r)$ of all orders are uniformly distributed over their domain, $0 \leq r \leq 1$. It is not hard to verify that for high orders and close to $r=0$, the $g_n(r)$ have values much greater than the polynomials $R_{nl}(r)$, as shown in the curves of Fig. 1. On the contrary, the values of $g_n(r)$ for $R_{nl}(r)$ close to zero and far away from it are bounded by ±1, even at high orders. Also,

Table 3 When $m_Z=4$, the numbers of complex and real moments are respectively 9 and 15. But if $m_g=4$, we obtain 25 complex and 45 real moments.

Polynomials with $n=l=m$	Number of complex moments, μ	Number of real moments, η
Zernike	$\sum_{i=0}^{m_Z}\left(\lfloor\frac{i}{2}\rfloor+1\right)$	$\dfrac{(m_Z+1)(m_Z+2)}{2}$
Fourier-Mellin, Chebyshev-Fourier, pseudo-Jacobi-Fourier	$(m_g+1)^2$	$2m_g^2+3m_g+1$

Table 4 The polynomials $g_n(r)e^{l\theta}$ in Euler form with real and imaginary parts for the orders $n=l=0,\ldots,3$. When $m_g=3$, one has $\mu=16$ and $\eta=28$.

		$g_n(r)e^{l\theta}$		
n	$l=0$	$l=1$	$l=2$	$l=m_g=3$
0	g_0	$g_0\cos\theta$	$g_0\cos 2\theta$	$g_0\cos 3\theta$
		$g_0\sin\theta$	$g_0\sin 2\theta$	$g_0\sin 3\theta$
1	g_1	$g_1\cos\theta$	$g_1\cos 2\theta$	$g_1\cos 3\theta$
		$g_1\sin\theta$	$g_1\sin 2\theta$	$g_1\sin 3\theta$
2	g_2	$g_2\cos\theta$	$g_2\cos 2\theta$	$g_2\cos 3\theta$
		$g_2\sin\theta$	$g_2\sin 2\theta$	$g_2\sin 3\theta$
$m_g=3$	g_3	$g_3\cos\theta$	$g_3\cos 2\theta$	$g_3\cos 3\theta$
		$g_3\sin\theta$	$g_3\sin 2\theta$	$g_3\sin 3\theta$

(a)

(b)

(c)

Fig. 2 Ronchigrams of a parabolic mirror as input images, grid resolution 8 lines/in., radius of curvature 2.0 m, and diameter 30.5 cm: (a) 5, (b) 7, and (c) 12 fringes.

as seen in Fig. 1(b), the zeros in the Zernike radial polynomials with high orders are uniformly distributed like the zeros of the polynomials $g_n(r)$. We remark that the retrieval of gray-level intensity distributions requires the computation of several high-order polynomials. Therefore, high values close to the center of an image produce high intensity levels that in binary images are imperceptible, but in gray-level images can be seen as a reconstruction artifact.

The reconstructed function $\hat{f}(r,\theta)$ can be computed using the infinite series

$$\hat{f}(r,\theta)=\sum_{n=0}^{\infty}\sum_{l=-\infty}^{\infty}A_{nl}p_{nl}(r,\theta). \tag{3}$$

If $l<0$ and $l\geq 0$, then Eq. (3) takes the form

$$\hat{f}(r,\theta)=\sum_{n=0}^{\infty}\sum_{-\infty}^{l<0}A_{nl}p_{nl}(r,\theta)+\sum_{n=0}^{\infty}\sum_{l\geq 0}^{\infty}A_{nl}p_{nl}(r,\theta)$$

$$=\sum_{n=0}^{\infty}\sum_{l>0}^{\infty}A_{n,-l}p_{n,-l}(r,\theta)+\sum_{n=0}^{\infty}\sum_{l\geq 0}^{\infty}A_{nl}p_{nl}(r,\theta)$$

$$=\sum_{n=0}^{\infty}\sum_{l>0}^{\infty}A_{nl}^{*}p_{nl}^{*}(r,\theta)+\sum_{n=0}^{\infty}\sum_{l\geq 0}^{\infty}A_{nl}p_{nl}(r,\theta)$$

$$=\sum_{n=0}^{\infty}\sum_{l>0}^{\infty}A_{nl}^{*}p_{nl}^{*}(r,\theta)+\sum_{n=0}^{\infty}\sum_{l>0}^{\infty}A_{nl}p_{nl}(r,\theta)$$

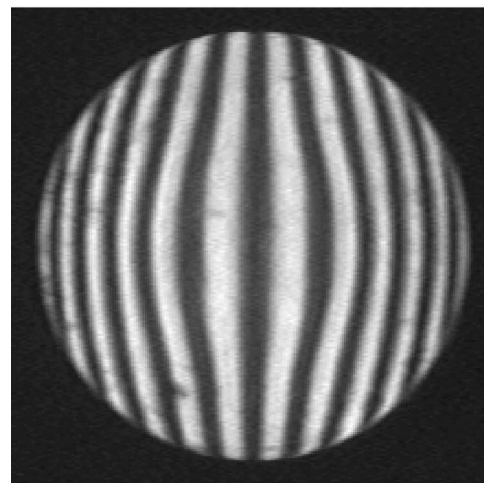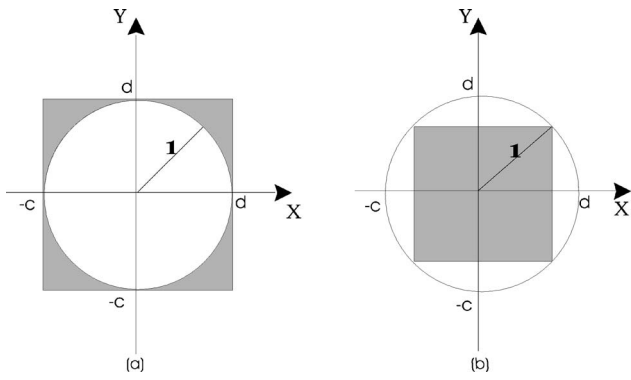$$+\sum_{n=0}^{\infty}A_{n0}\begin{Bmatrix}R_{n0}(r)\\g_n(r)\end{Bmatrix}, \tag{4}$$

where $A_{nl}^{*}p_{nl}^{*}(r,\theta)=A_{n,-l}p_{n,-l}(r,\theta)$. However, we can limit the number of terms in the series expansion to $n=0,1,2,\ldots,m$ and $l=0,1,2,\ldots,m$. Here, both the radial and harmonic order maxima are denoted by m. It is easily verified that Eq. (4) can be written as

Fig. 3 Coordinate transformations of an image to the unit circle: (a) outside, $c=d=1$; (b) inside, $c=d=\sqrt{2}$, $d=\sqrt{1/2}$.

$$\hat{f}(r,\theta) = 2\sum_{n=0}^{m}\sum_{l>0}^{m}(\mathrm{Re}\,A_{nl}\cos l\theta - \mathrm{Im}\,A_{nl}\sin l\theta)\begin{Bmatrix}R_{nl}(r)\\g_n(r)\end{Bmatrix}$$
$$+\sum_{n=0}^{m}(\mathrm{Re}\,A_{n0} + i\,\mathrm{Im}\,A_{n0})\begin{Bmatrix}R_{n0}(r)\\g_n(r)\end{Bmatrix}, \qquad (5)$$

where the Euler formula $e^{il\theta}=\cos l\theta + i\sin l\theta$ and $A_{nl}=\mathrm{Re}A_{nl}+i\,\mathrm{Im}A_{nl}$ have been used. The real series expansion is given by

$$|\hat{f}(r,\theta)| = 2\sum_{n=0}^{m}\sum_{l>0}^{m}(\mathrm{Re}\,A_{nl}\cos l\theta - \mathrm{Im}\,A_{nl}\sin l\theta)\begin{Bmatrix}R_{nl}(r)\\g_n(r)\end{Bmatrix}$$
$$+\sum_{n=0}^{m}[(\mathrm{Re}\,A_{n0})^2 + (\mathrm{Im}\,A_{n0})^2]^{1/2}\begin{Bmatrix}R_{n0}(r)\\g_n(r)\end{Bmatrix}. \qquad (6)$$

We have to take into account that there are significant

Table 5 Reconstruction of the image of Fig. 2(a) with all possible alternatives. Before reconstruction was performed, the input image was resized to 54×54 px. The reconstructed image contrast using Fourier-Mellin, Chebyshev-Fourier, and pseudo-Jacobi-Fourier moments is much lower than using Zernike moments. The reconstructions orders are 10 (20), 15 (30), and 20 (40).

Table 6 The contrast is achieved better in some of the reconstructed images. Afterward $|\hat{f}|^2$ or $|\hat{f}|$ was computed, we compressed the dynamic range with the usual log transformation to visualize the intensity distributions. Only the reconstructed images using the Zernike moments has not been so transformed.

Moments	Coordinate Transformation	Square $\left|\hat{f}\right|^2$			Module $\left|\hat{f}\right|$		
		20	30	40	20	30	40
Zernike	Outside						
	Inside						
		10	15	20	10	15	20
Mellin Fourier	Outside						
	Inside						
Chebyshev Fourier	Outside						
	Inside						
Pseudo Jacobi Fourier	Outside						
	Inside						

differences in the numbers of terms obtained in the series of Eq. (6), using the same number m for the polynomials $R_{nl}(r)$ and $g_n(r)$. This fact is due to the constraints imposed on n and l in the Zernike polynomial definition, so that a given value of m produces more terms in the series for $g_n(r)$ than for $R_{nl}(r)$, as shown in Table 2. The number μ of complex moments A_{nl} in Eq. (3) and the total number η of polynomials $\sin l\theta$, $\cos l\theta$, and $R_{n0}(r)$ used in Eq. (6) can be computed with the formulas provided in Table 3. The formulas for Zernike polynomials have been published in Ref. 11 and 22. In the case of Fourier-Mellin, Chebyshev-Fourier, and pseudo-Jacobi-Fourier polynomials, similar formulas can be obtained using Table 4.

3 Reconstruction of Grayscale Images

In optical workshops a common test used to determine the quality of optical surfaces is the Ronchi test.[11] During the polishing process, the surface quality is continuously verified, and the interferometric verification procedure requires images of the surface under testing; these images are currently known as Ronchigrams. Here, we used three Ronchigrams and their grayscale images to evaluate the reconstruction capabilities of the orthogonal moments described in the previous section. The Ronchigrams used for this work are shown in Fig. 2. These images have different spatial frequency, and finding their center is an important step; a bad reconstruction of these fringes in the pattern would decrease the accuracy of the test.

3.1 Discrete Orthogonal Moments of an Image and Its Reconstruction

Let $f(r_{ij}, \theta_{ij})$ be a digital image with spatial dimensions $M \times N$. Its discrete moments A_{nl} are given by
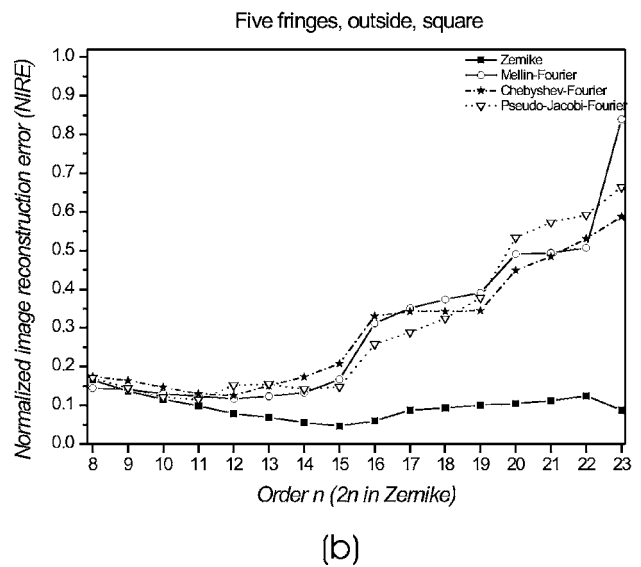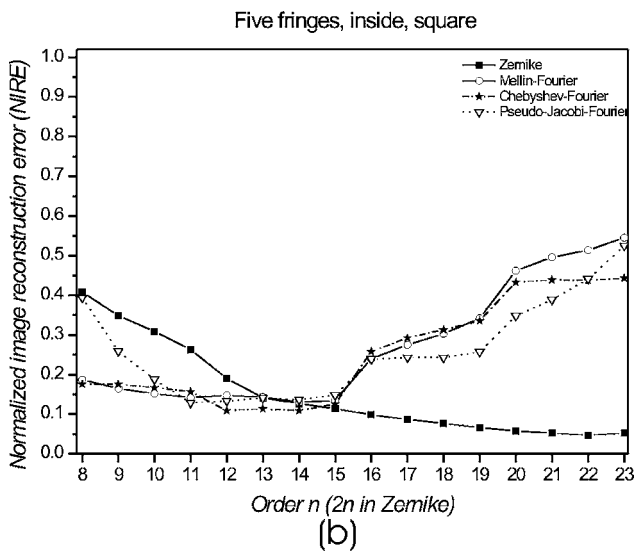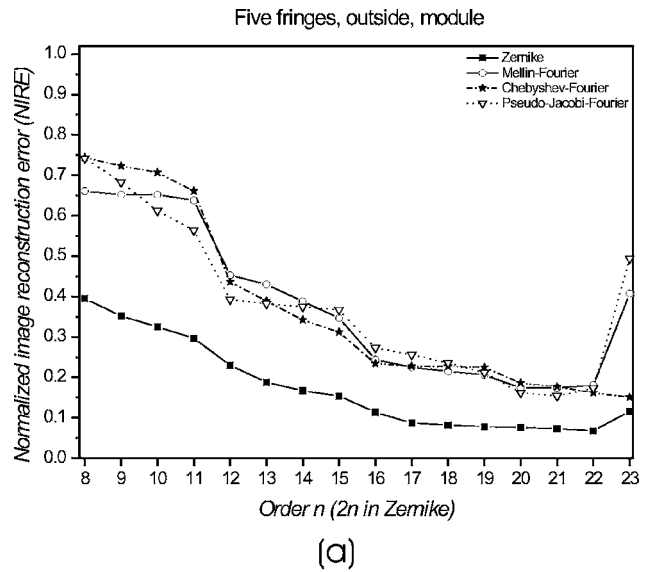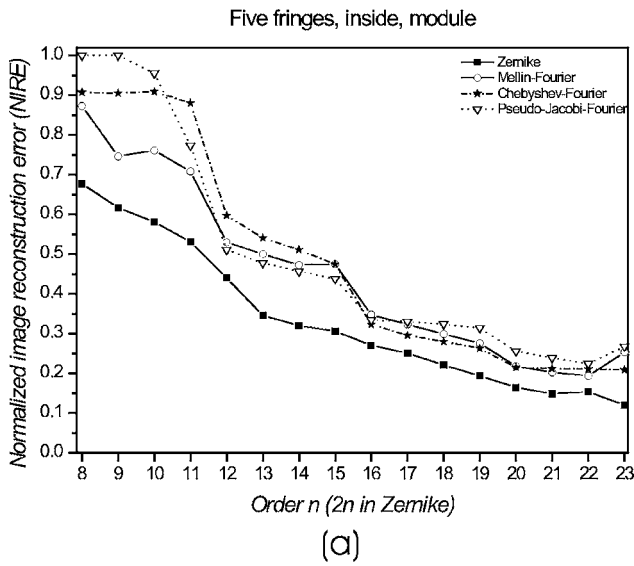
Fig. 4 NIRE of the Ronchigram with five fringes, using all moment sets. The input image has been previously mapped inside the unit circle. For the Zernike moments the order is $2n$, and the reconstructed distributions were obtained with (a) $|\hat{f}|$ and (b) $|\hat{f}|^2$.

Fig. 5 NIRE of the Ronchigram with five fringes, using all moment sets. The input image has been previously mapped outside the unit circle. For the Zernike moments the order is $2n$, and the reconstructed distributions were obtained with (a) $|\hat{f}|$ and (b) $|\hat{f}|^2$.

$$A_{nl} = \kappa_n \sum_{i=0}^{M-1} \sum_{j=0}^{N-1} f(r_{ij}, \theta_{ij}) \begin{Bmatrix} R_{nl}(r_{ij}) \\ g_n(r_{ij}) \end{Bmatrix} \exp(il\theta_{ij}), \qquad (7)$$

where the discrete polar coordinates

$$r_{ij} = [x_j^2 + y_i^2]^{1/2}, \qquad \theta_{ij} = \arctan\left(\frac{y_i}{x_j}\right) \qquad (8)$$

are transformed by

$$x_j = c + \frac{j(d-c)}{N-1}, \qquad y_i = d - \frac{i(d-c)}{M-1}. \qquad (9)$$

Here, the index variables, $i=0,\ldots,M-1$ and $j=0,\ldots,N-1$ represent the rows and columns of the image data matrix. The real numbers c and d take different values according as

the image function is mapped outside or inside the unit circle, as shown in Fig. 3. As in the continuous case, the radial and harmonic orders are respectively $n = 0, 1, 2, \ldots, m$ and $l = 0, 1, 2, \ldots, m$.

The reconstructed complex discrete distribution of the image is given by

$$\hat{f}(r_{ij}, \theta_{ij}) = \sum_{n=0}^{m} \sum_{l=0}^{m} A_{nl} \begin{Bmatrix} R_{nl}(r_{ij}) \\ g_n(r_{ij}) \end{Bmatrix} \exp(il\theta_{ij}), \qquad (10)$$

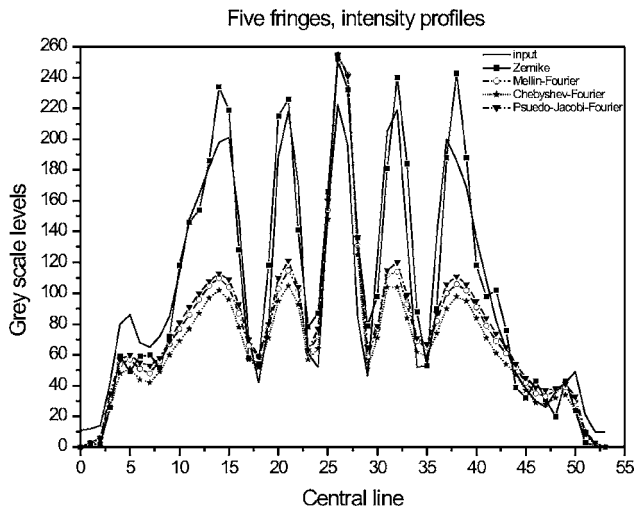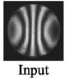its amplitude distribution is obtained from $|\hat{f}|$, and its intensity distribution from $|\hat{f}|^2$.

Fig. 6 Intensity profiles along row 27 of the reconstructed images with order $n=l=15$ (30), using all moment sets. The input image size is 54×54 px, and its rms contrast is 0.256. For Zernike, Fourier-Mellin, Chebyshev-Fourier, and pseudo-Jacobi-Fourier polynomials, the rms contrasts are respectively 0.274, 0.326, 0.348, and 0.315.

Fig. 7 NIRE of the Ronchigram with seven fringes, using all moment sets. The input image has been mapped outside the unit circle. The reconstructed intensity distributions were obtained with $|\hat{f}|^2$. For the Zernike moments the order is $2n$ and the optimum reconstruction interval with the minimum NIRE for all sets is. [Refs. 12 and 15]

3.2 Image Quality Metrics

In this subsection we review some basic metrics of image quality for use in comparing the images under study. The first one is the *normalized image reconstruction error* (NIRE) between an input image $f(i,j)$ and its reconstruction $\hat{f}(i,j)$.[7,8] It is defined by the following equation for two images of spatial dimensions $M \times N$:

$$\mathrm{NIRE} = \frac{\sum_{i=0}^{M-1} \sum_{j=0}^{N-1} [f(i,j) - \hat{f}(i,j)]^2}{\sum_{i=0}^{M-1} \sum_{j=0}^{N-1} \hat{f}^2(i,j)}. \tag{11}$$

Table 8 Reconstructions of the input image of Fig. 2(b) for orders 12 to 15. Before the reconstructions were performed, the input image was resized to 110×110 px. Again for OFMM, CHFM, and PJFM, the log transformation has been used to visualize the intensity distributions $|\hat{f}|^2$. Only the Zernike moments can retrieve all the fringes in the image with good contrast.

Table 7 Spatial frequency S_{freq} as a measurement of the contrast.

Image	C_{freq}	R_{freq}	S_{freq}
Input	15.288	35.628	38.769
Zernike (30)	13.035	30.27	32.957
Mellin-Fourier (15)	8.994	13.164	15.943
Chebyshev-Fourier (15)	8.572	12.758	15.37
Pseudo-Jacobi-Fourier (15)	9.057	13.269	16.066

Moments	12	13	14	15
Zernike				
Melin-Fourier				
Chebyshev-Fourier				
Pseudo-Jacobi-Fourier				

Fig. 8 Intensity profiles along row 55 of the reconstructed images with order $n=l=15$ (30), using all moment sets. The input image size now is 110×110 px, and its rms contrast is 0.201. For Zernike, Fourier-Mellin, Chebyshev-Fourier, and pseudo-Jacobi-Fourier plynomials, the rms contrasts are respectively 0.197, 0.179, 0.181, and 0.179. Only the curve of the Zernike reconstruction follows the profile of the input image.

Usually, digitally captured images are corrupted by noise produced by the image acquisition system, and a way to estimate the amount of noise in the acquired image, $f_{\text{noisy}}(i,j)$, is by computing its histogram to determine the values of the mean μ as well as the variance σ^2 of the grayscale image.[23] These statistical quantities are defined as follows:

$$\mu = \sum_{i=0}^{M-1} \sum_{j=0}^{N-1} f_{\text{noisy}}(i,j) \text{h}_N[f_{\text{noisy}}(i,j)] \tag{12}$$

and

$$\sigma^2 = \sum_{i=0}^{M-1} \sum_{j=0}^{N-1} [f_{\text{noisy}}(i,j) - \mu]^2 \text{h}_N[f_{\text{noisy}}(i,j)], \tag{13}$$

where $\text{h}_N[f_{\text{noisy}}(i,j)] = \text{h}[f_{\text{noisy}}(i,j)]/MN$ are the normalized histogram values.

Also, the image contrast can be used to compare two different grayscale images; a common technique is to use the *root mean square* (rms) contrast.[24,25] If the rms contrast is the same in both grayscale images, then they have the same contrast. It is defined as

$$\text{RMS} = \left[\frac{1}{MN} \sum_{i=0}^{M-1} \sum_{j=0}^{N-1} [f_N(i,j) - \bar{f}_N(i,j)]^2 \right]^{1/2}, \tag{14}$$

where $f_N(i,j) = f(i,j)/255$ denotes the *normalized grayscale image* $f(i,j)$, and $\bar{f}_N(i,j)$ represents the *mean normalized grayscale image* given by

$$\bar{f}_N(i,j) = \frac{1}{MN} \sum_{i=0}^{M-1} \sum_{j=0}^{N-1} f_N(i,j). \tag{15}$$

Table 9 Reconstructions of the input image of Fig. 2(c) using all the moment sets for order $n=l=40$. The size of the input image is 220×220 px. For OFMM, CHFM, and PJFM the log transformation has been used to visualize the intensity distributions $|\hat{f}|^2$. Only the Zernike moments can retrieve all the fringes in the image with good contrast.

Moments	$n = l = 40$
Zernike	
Mellin-Fourier	
Chebyshev-Fourier	
Pseudo-Jacobi-Fourier	

Contrast can also be based on spatial frequency;[26,27] hence, as a measure of overall activity in a grayscale image $f(i,j)$, it is defined by

$$S_{\text{freq}} = (R_{\text{freq}}^2 + C_{\text{freq}}^2)^{1/2}, \tag{16}$$

where R_{freq} and C_{freq} are, respectively, the row and column frequencies of the image, which are computed by

$$R_{\text{freq}} = \left(\frac{1}{MN} \sum_{i=0}^{M-1} \sum_{j=0}^{N-1} [f(i,j) - f(i,j-1)]^2 \right)^{1/2} \tag{17}$$

and

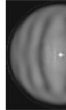$$C_{\text{freq}} = \left(\frac{1}{MN} \sum_{i=0}^{M-1} \sum_{j=0}^{N-1} [f(i,j) - f(i-1,j)]^2 \right)^{1/2}. \tag{18}$$
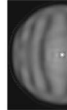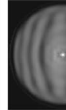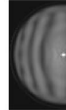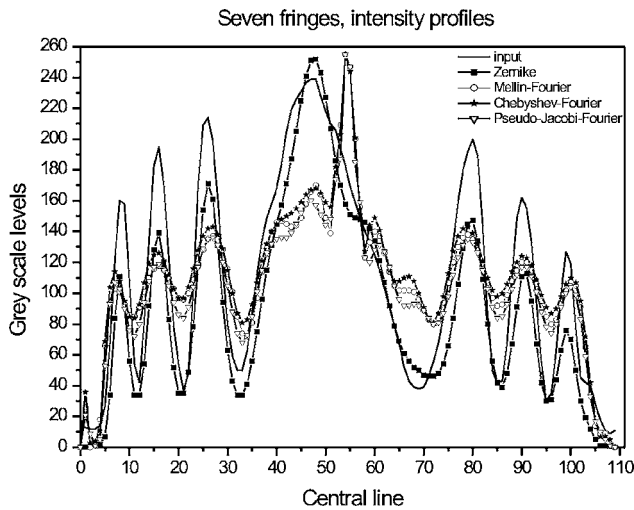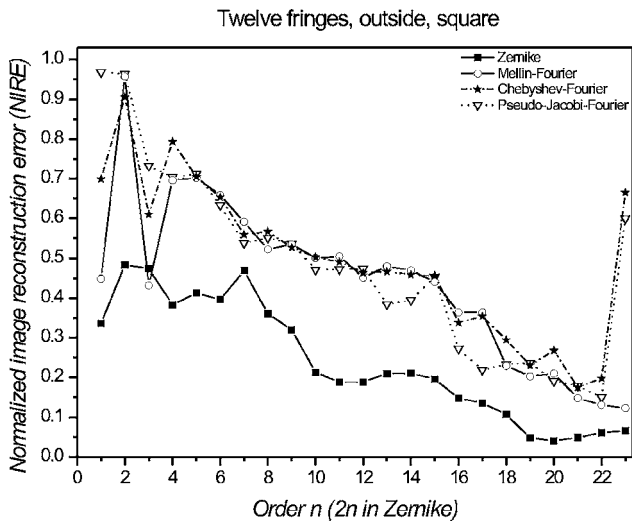
Fig. 9 NIRE of the Ronchigram with 12 fringes, using all moment sets. The input image has been mapped outside the unit circle. The reconstructed intensity distributions were obtained with $|\hat{f}|^2$. For the Zernike moments, the order is $2n$. The minimum NIREs for all sets are presented up to the 40th order, and only the Zernike moments are able to retrieve all fringes.
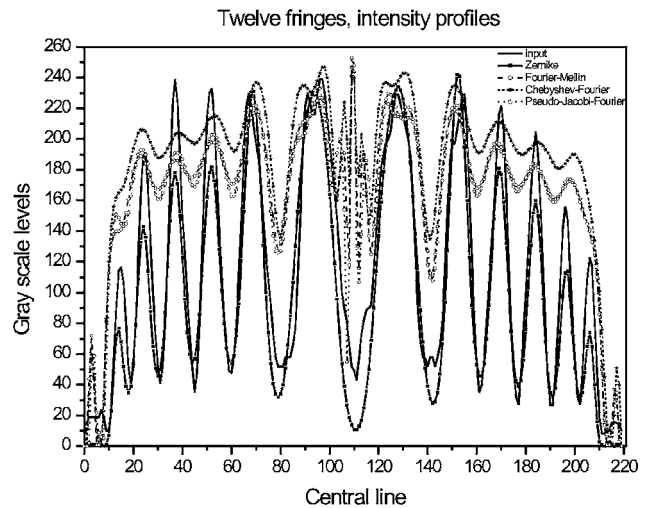

Fig. 10 Intensity profiles along row 110 of the reconstructed images with order $n=l=20$ (40) using all moment sets. The size of the input image is 220×220 px, and its rms contrast is 0.06. For Zernike, Fourier-Mellin, Chebyshev-Fourier, and pseudo-Jacobi-Fourier polynomials, the contrasts are respectively 0.088, 0.433, 0.502, and 0.433. Only the curve of the Zernike reconstruction follows the profile of the input image.

3.3 Digital Reconstruction

In the present subsection, we display the reconstructions of the Ronchigram images using the moment sets described in Sec. 2. Before the reconstructions are performed, the two coordinate transformations proposed in Sec. 3.1 are applied to the input images of Fig. 2. The first transformation is made by setting $c=-1$ and $d=+1$ in Eq. (9); therefore the image is mapped outside the unit circle. For the second mapping, the values c and d are, respectively, $-1/\sqrt{2}$ and $+1/\sqrt{2}$, and consequently the input image is now transformed inside the unit circle.

According to the analysis provided in Sec. 2, we show in Table 5 the reconstructed images of Fig. 2(a), using the orders $n=l=20,30,40$ for the Zernike moments and $n=l=10,15,20$ for the OFM, CHF, and PJF moments. Also in Table 5, the intensity and amplitude distributions of the reconstructed images are displayed, using respectively the square $|\hat{f}|^2$ and the modulus $|\hat{f}|$ of the complex reconstructed distribution $\hat{f}$. In all cases of reconstruction performed by OFMM, CHFM, and PJFM, the resulting image contrast is low. Thus, each grayscale image has been processed with a log transformation to compress its dynamic range within the same data matrix in order to improve its contrast, as illustrated in Table 6. It is clear that image contrast is enhanced in comparison with the nontransformed images shown in Table 5. In Table 6, it can be observed that reconstruction results closer to the input image are obtained using $|\hat{f}|^2$, for orders between 15 (30) and 20 (40), where the second number within parentheses is the order of the Zernike moments and the first number is the order for the other moment sets.

The NIREs are graphed in Figs. 4 and 5 using the orders $n=l=16,18,20,\ldots,40$ for the Zernike moments and $n=l=8,9,10,\ldots,20$ for the OFM, CHF, and PJF moments.

Another interesting comparison can be made by considering the contrast of the reconstructed fringes. The central intensity profiles of the input and the reconstructed images of Table 6 for orders $n=l=15$ (30), using $|\hat{f}|^2$ and the outside coordinate transformation, are shown in Fig. 6. As a second contrast measure, we have used Eqs. (16)–(18); these are shown in Table 7.

In the second case of reconstruction, the Ronchigram has seven fringes as shown in the input image of Fig. 2(b). The NIREs obtained for all moment sets are graphed in Fig. 7, from which it is not hard to verify that the best reconstructed images are in the interval 24 to 30 for Zernike polynomials and 12 to 15 for OFMM, CHFM, and PJFM. To show the advantage of using the Zernike moments in Ronchigram reconstruction, the reconstructed images with the lowest NIREs are shown in Table 8. Our results have been obtained using the squared intensity distributions, the outside mapping, and the log transformation for the polynomials $g_n(r)$. As in the first example, the central intensity profiles are graphed for the input and the reconstructed images using the orders $n=l=15$ (30), as shown in Fig. 8. The row spatial frequency R_{freq} of the input image was computed; its value is 20.992. For the reconstructed images the R_{freq} values are, respectively, 14.021, 9.073, 9.408, and 9.011 for Zernike, OFMM, CHFM, and PJFM.

Some intensity distributions of the third reconstructed image with the orthogonal moments are shown in Table 9. It is an interesting case in that the input image has 12 fringes and only the Zernike moments are able to reconstruct all of them. The graphs of the NIRE and their intensity central profiles are shown, respectively, in Figs. 9 and 10. The orders $n=l=2,4,6,\ldots,46$ for the Zernike moments and $n=l=1,2,3,\ldots,23$ for the other sets have been used. As in the previous cases, R_{freq} is also computed. For
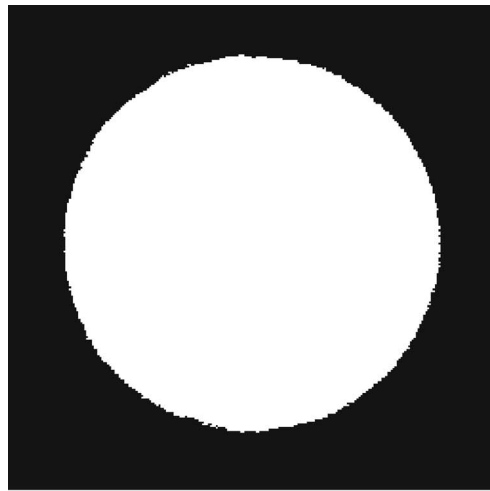
(a)
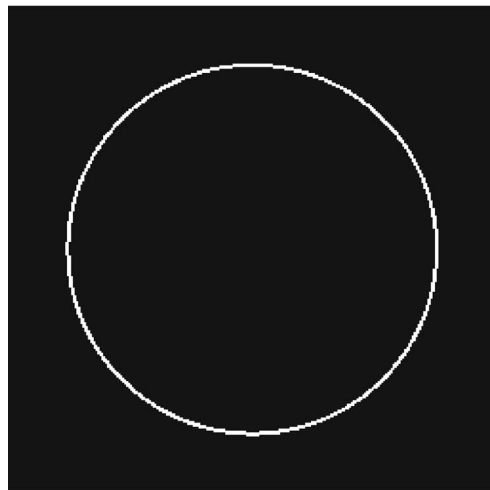
(b)
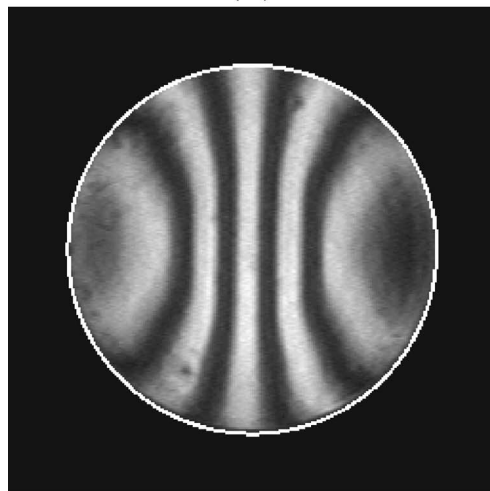
(c)

Fig. 11 (a) Binary image of the Ronchigram with five fringes thresholded with a value of 19. (b) Circle with 98 px as radius, obtained with geometric moments. (c) Circle around the original Ronchigram as the first zone to be filtered.
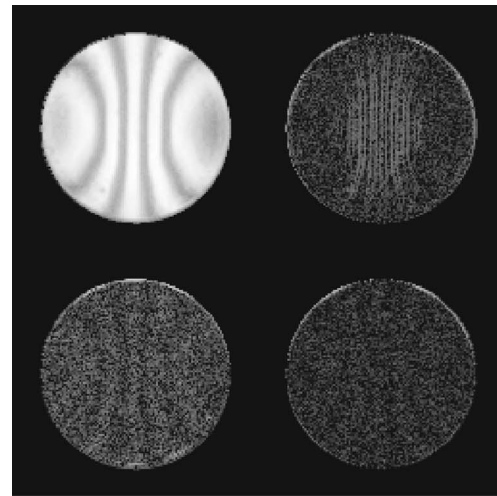
(a)
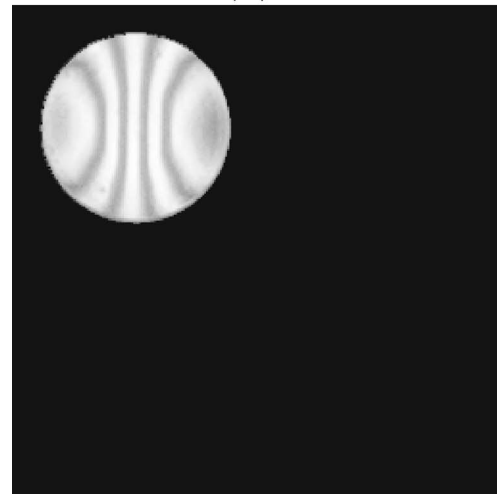
(b)
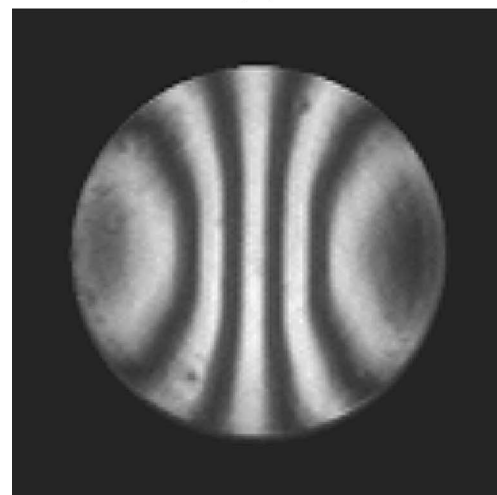
(c)

Fig. 12 (a) Multiresolution analysis of the Ronchigram with five fringes using the first level of the Daubechies wavelet transform with kernel Daub(4). (b) Filtering of the image transform using the elimination rule. (c) Inverse wavelet transform to obtain the reference image $f_R(i,j)$.

Input   Reference   Noise
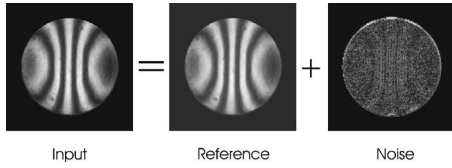
Fig. 13 Denoising the input image to obtain a filtered reference image.

the input image, the value is 19.081; for the Zernike, OFM, CHF, and PJF the values obtained are, respectively, 14.01, 9.26, 10.34, and 9.16.

All input test images presented here have been slightly corrupted by noise during digital acquisition; for this reason, the NIRE cannot always be reduced by increasing the number of moments. The NIRE curves show random behavior in some parts of the order (n) axis. If a noisy image is reconstructed, only a few moments generate the minimum NIRE. Amu et al.[10] stated a relationship for the signal-to-noise ratio of a noisy image $f(r, \theta)$ as follows:

$$\text{SNR}_{\text{input}} = \frac{k^2}{A\sigma^2} \int_0^{2\pi} \int_0^k f_{\text{noisy}}^2(r, \theta) r \, dr \, d\theta, \quad (19)$$

where σ is the standard deviation of the noise, A is the area of the image, and k its scale. In Sec. 5, we discuss a method used to reduce noise in a Ronchigram image, based on the Daubechies wavelet transform. Since the area A of the Ronchigram is required in Eq. (19), it can be obtained using the geometric moments of the image as described in the next section.

4 Circles and Geometric Moments

In this section we obtain the area and the radius of the Ronchigrams used as grayscale test images; a threshold value is used to binarize the gray-level image under consideration. Obviously, due to the circular aperture used to capture a Ronchigram image, its binarization produces a circle. Geometric moments are implemented to obtain the area of the binarized image, and from it the corresponding radius is computed.[28] The geometric moments m_{pq} of order $p+q$ of a binary image $B(x_i, x_j)$ are defined as

$$m_{pq} = \sum_{i=0}^{M-1} \sum_{j=0}^{N-1} x_i^p y_j^q B(x_i, x_j), \quad (20)$$

where $B(x_i, x_j)$ takes the value 255 or 0 and $M \times N$ is the image size. By definition, the moment of order zero, m_{00}, represents the total intensity in the image, and the point $(m_{10}/m_{00}, m_{01}/m_{00}) = (\bar{x}, \bar{y})$ is the intensity centroid. We can define a family of circles $C(k)$ by the equation

$$(x - \bar{x})^2 + (y - \bar{y})^2 = \frac{km_{00}}{255\pi}, \quad (21)$$

where $0 < k \leq 1$ represents the scale of the circle and $m_{00}/255$ is its area in pixels. The radius of the image is given by

$$r = \left(\frac{km_{00}}{255\pi}\right)^{1/2}, \quad (22)$$

where the factor $1/255$ is introduced to normalize the circle area. A Ronchigram image with a circle drawn around it is shown in Fig. 11. For digital purposes the integer part $\lfloor r \rfloor$ is used instead of r; all pixels inside the circle of radius 98 are filtered.

5 Noise Removal with Wavelet

Noise in an image acquisition system generally exists due to random fluctuations in the electrical signal from the detector to the framegrabber or in the analog-to-digital converter. The ability of the sensor to detect small amounts of radiant energy may be inhibited by the presence of noise during the detection process and in certain environments; these little differences of radiant energy may change the image reconstruction process as illustrated in the preceding section. The orthogonal moments of the noisy image are a combination of the object and the noisy moments. Our Ronchigrams have been acquired by a CCD sensor, and it introduces enough noise to affect the reconstruction of the images. Noise can only be removed partially, because it is generally impossible to filter out all noise present in the image without modifying its spatial frequency content. In particular, we are interested in quantifying the noise of the input images, and for that purpose a reference image is obtained using the Daubechies wavelet transform. In the following section, a quantitative analysis is carried out to compute the SNR of the input test image.

5.1 Quantitative Analysis of Noise

This section briefly describes the method of noise removal using the wavelet transform.[29–33] At each stage of the transformation, the image is decomposed into four quarter-size images, as shown in Fig. 12(a), resulting from the input image of Fig. 11(c). The circle does not contribute in any way to obtaining the wavelet transform; it is only a picture, used primarily to filter noise. To obtain the discrete wavelet transform $f_2^i(m, n)$ with $i = 0, 1, 2, 3$ of an input image $f_1(m, n)$, an orthogonal multiresolution basis with compact support has been used with the symmetric Daubechies wavelet family.[30]

In the wavelet transform plane a coefficient elimination rule is implemented to filter out noise,[33] as follows:
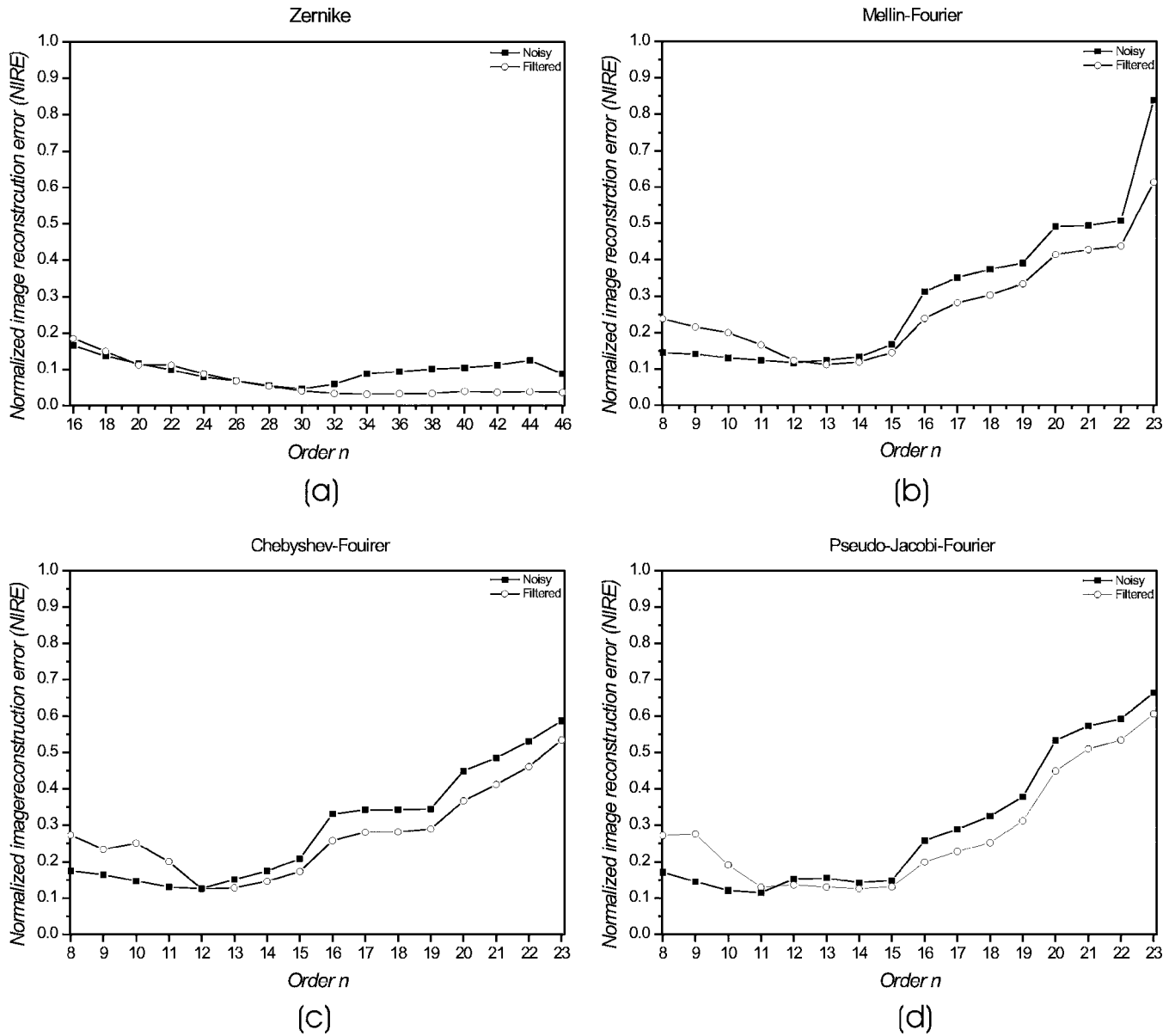
$$f_2^i(m, n) = 0 \quad (23)$$

Fig. 14 NIRE for the input and filtered (reference) images, using all moment sets, for orders $n=l$ $=8(16),\ldots,23(46)$. (a) Zernike, (b) Fourier-Mellin, (c) Chebyshev-Fourier, and d) pseudo-Jacobi-Fourier.

along directions $i=1,2,3$, as shown in Fig. 12(b). These directions are selected according to the amount of noise required to be eliminated in each direction. A 2-D inverse process is obtained via the *inverse discrete wavelet transformation*.[29,31] A reference filtered image $f_R(i,j)$ as shown in Fig. 12(c) is obtained from the image of Fig. 12(b), using its inverse wavelet transformation.

Many reference images can be obtained using the kernels of the Daubechies family. Here we used the Daub(4) kernel, which was selected in order to get the highest SNR. The noise filtered from the input image to obtain the reference is shown in Fig. 13. The highest spatial frequencies have been eliminated from the input and are found in the image labeled "Noise." After the reference image is obtained, it can be used as a new input image in the process of reconstruction using all moment sets.

The new behavior of the NIRE is shown in Fig. 14. The curves indicate that high orders are more sensitive to noise. For a given noisy image $f_{\text{noisy}}(i,j)$ there is an $\text{SNR}_{\text{input}}$ that generates an optimum number of moments suitable to minimize the NIRE.

Our interest in this subsection is to evaluate the amount of noise that was filtered to obtain the reference image. Beginning with the image of five fringes given in Fig. 11(c) and rewriting Eq. (19), we get

$$\text{SNR}_{\text{input}} \approx \frac{k^2 I}{A\sigma^2}, \tag{24}$$

where I can be computed as

$$I = \sum_{i=0}^{M-1} \sum_{j=0}^{N-1} f_{\text{noisy}}^2(i,j). \tag{25}$$

To evaluate Eq. (24) only the pixels inside the circle in the interval $0 \leq r_{ij} \leq k$ are considered. Letting the value of the scale be $k=1$, the image of Fig. 11(c) has area $A_{\text{input}} = 3.056 \times 10^4$ px, and $I_{\text{input}} = 4.777 \times 10^9$ px. Equation (24) then takes the form

$$SNR_{\text{input}} = \frac{\text{const}}{\sigma^2}, \tag{26}$$

where const$=1.563 \times 10^5$. The variance in the input image can be obtained using Eqs. (12) and (13); its value is $\sigma_{\text{input}}^2 = 4.737 \times 10^3$, and $SNR_{\text{input}} = 32.998$. A similar procedure is followed for the reference image with the same area; in this case, the values obtained are $I_{\text{reference}} = 5.716 \times 10^9$, const$=1.87 \times 10^5$, $\sigma_{\text{reference}}^2 = 3.859 \times 10^3$, and $SNR_{\text{reference}} = 48.473$.

6 Conclusions

We have reconstructed gray-level images with simple structure, such as Ronchigrams, using the four orthogonal moment sets reviewed in Sec. 2. The performance of these moments in image reconstruction has been measured by image quality metrics such as the NIRE, rms contrast, spatial frequency, and SNR. These measures lead us to conclude that the Zernike moments are better than OFMM, CHFM, and PJFM for describing gray-level images of interference patterns.

The NIRE can be lowered using digital image-processing techniques and geometrical transformations. Also, noise reduction in the input image is substantially important for high-order moments, as was shown in Fig. 14. It is clear that the reconstruction of Ronchigrams with many fringes, as illustrated in the third example of Sec. 3.3, depends on the high spatial frequencies involved. In this case of 12 fringes, the mixture of high and low frequencies produces abrupt changes, and the image reconstruction requires moments of high order. Only polynomials with high orders and homogeneous distributions of zeros, and without very large values near the domain boundaries, can reconstruct the original function without artifacts. As has been shown, only the Zernike polynomials maintain these conditions. The contrast in the reconstructed Ronchigrams has been approximately retrieved, and again the Zernike moments give better contrast than the other sets of moments.

In general, the optimum number of moments to get a minimum NIRE depends on the spatial frequencies and the noise involved in the grayscale image. For the interference patterns presented here the optimum number is around 15 (30) for 5 and 7 fringes, and around 20 (40) for 12 fringes. Higher orders are required for interference patterns with more fringes. On the other hand, it has been shown that the reconstruction errors attain the lowest values when the input image is previously mapped outside the unit circle. The NIRE of the intensity distributions of the reconstructed images can be lowered using $|f|^2$. Based on the results obtained, the Zernike moments are superior for the Ronchigram reconstruction to the other moment sets.

References

1. S. O. Belkasin, "Pattern recognition with moment invariants—a comparative study and new results," *Pattern Recogn.* **24**(12), 1117–1138 (1991).
2. C. Kan and M. D. Srinath, "Invariant character recognition with Zernike and orthogonal Fourier-Mellin moments," *Pattern Recogn.* **35**, 143–154 (2002).
3. R. J. Prokop and A. P. Reeves, "A survey of moment-based techniques for unoccluded object representation and recognition," *CVGIP: Graph. Models Image Process.* **54**, 438–460 (1992).
4. A. Khotanzad, "Object recognition using a neural network and invariance Zernike features," in *Int. Conf. on Computer Vision and Pattern Recognition*, pp. 200–207, IEEE Computer Soc. (1989).
5. M. K. Hu, "Visual pattern recognition by moment invariants," *IRE Trans. Inf. Theory* **IT-8**, 179–187 (1962).
6. M. R. Teague, "Image analysis via the general theory of moments," *J. Opt. Soc. Am.* **70**, 920–930 (1980).
7. Y. L. Sheng and L. X. Shen, "Orthogonal Fourier-Mellin moments for invariant pattern recognition," *J. Opt. Soc. Am. A* **11**, 1748–1757 (1994).
8. Z. L. Ping, R. G. Wu, and Y. L. Sheng, "Image description with Chebyshev-Fourier moments," *J. Opt. Soc. Am. A* **19**, 1748–1754 (2002).
9. R. Mukundan and K. R. Ramakrishnan, *Moment Functions in Image Analysis*, World Scientific, Singapore (1998).
10. G. Amu, S. Hasi, X. Yang, and Z. Ping, "Image analysis by pseudo-Jacobi ($p=4$, $q=3$)-Fourier moments," *Appl. Opt.* **43**, 2093–2101 (2004).
11. A. Cornejo-Rodríguez, "Ronchi test," Chap. 10 in *Optical Shop Testing*, D. Malacara, Ed., 2nd ed., John Wiley and Sons, New York (1992).
12. A. B. Bhatia and E. Wolf, "On circular polynomials of Zernike and related orthogonal sets," *Proc. Cambridge Philos. Soc.* **50**, 40–48 (1954).
13. C. Chong, P. Raveendran, and R. Mukundan, "A comparative analysis of algorithms for fast computation of Zernike moments," *Pattern Recogn.* **36**, 731–742 (2003).
14. C. Chong, P. Raveendran, and R. Mukundan, "Translation invariants of Zernike moments," *Pattern Recogn.* **36**, 1765–1773 (2003).
15. A. K. Jain, *Fundamentals of Digital Image Processing*, Prentice-Hall (1989).
16. W. K. Pratt, *Digital Image Processing*, 2nd ed., John Wiley and Sons, New York (1991).
17. S. G. Tyan, "Median filtering, deterministic properties," in *Two-Dimensional Digital Signal Processing*, T. S. Huang, Ed., Vol. II, Springer-Verlag, Berlin (1981).
18. N. Becerer, H. Jodicke, G. Schlosser, J. Hesser, F. Zeilfelder, and R. Manner, "On soft clipping of Zernike moments for deblurring and enhancement of optical point spread functions," in *Proc. SPIE* **6065**, 60650C-1-11 (2006).
19. R. Mukundan, "Image analysis by Tchebichef moments," *IEEE Trans. Image Process.* **10**(9), 1357–1364 (2001).
20. P. T. Yap and R. Paramesan, "Image analysis by Krawtchouk moments," *IEEE Trans. Image Process.* **12**(11), 1367–1377 (2003).
21. N. Hueber, B. Colicchio, A. Dieterlen, and S. Jacques, "Zernike polynomial applications in 3D fluorescence microscopy," *Journeé du CRESPIM*, Mulhouse, France (2003).
22. E. Micheli-Tzanakou, *Supervised and Unsupervised Pattern Recognition*, pp. 90–96, CRC Press, Boca Raton, FL (2000).
23. R. C. Gonzalez and R. E. Woods, *Digital Image Processing*, 2nd ed., Prentice-Hall, (2002).
24. E. Peli, "Contrast in complex images," *J. Opt. Soc. Am. A* **7**, 2032–2040 (1990).
25. A. M. Eskicioglu and P. S. Fisher, "Image quality measures and their performance," *IEEE Trans. Commun.* **43**, 2959–2965 (1995).
26. S. Yi, J. T. Kwok, and Y. Wan, "Combination of images with diverse focus using the spatial frequency," *Inf. Fusion* **2**, 169–176 (2001).
27. A. Sluzek, "Identification and inspection of 2-D objects using new moment-based shape descriptors," *Pattern Recogn. Lett.* **16**, 687–697 (1995).
28. I. Daubechies, *Ten Lectures on Wavelets*, SIAM Press, Philadelphia (1992).
29. M. Pavel, G. Sperling, T. Riedl, and A. Vanderbeek, "Limits of visual communications: the effect of signal-to-noise ratio on the intelligibility of American Sign Language," *J. Opt. Soc. Am. A* **4**, 2355–2365 (1987).
30. K. R. Castleman, *Digital Image Processing*, Prentice-Hall (1996).

31. S. G. Mallat, "A theory for multi-resolution signal decomposition in the wavelet representation," *IEEE Trans. Pattern Anal. Mach. Intell.* **11**(7), 674–693 (1989).
32. C. S. Burrus, R. A. Gopinath, and H. Guo, *Introduction to Wavelets and Wavelet Transforms*, Prentice-Hall, (1998).
33. J. Torres and S. O. Infante, "Wavelet analysis for the elimination of striping noise in satellite images," *Opt. Eng.* **40**(7), 1309–1314 (2001).

Alfonso Padilla-Vivanco received his physics degree in 1994 from Puebla Autonomous University, Mexico, and his MS degree in 1995 and his PhD degree in 1999, both in optics, from the National Institute of Astrophysics, Optics, and Electronics. In 2000, he held a postdoctoral position in the Physics Department at the University of Santiago de Compostela, Spain. He is now a researcher from Polytechnic University of Tulancingo, Hidalgo, Mexico. His research interests include optical information processing, image analysis, and computer vision.

Gonzalo Urcid-Serrano received his basic degree in electronics and computer engineering in 1982 and his MS degree in computer sciences in 1985, both from the University of the Americas, Mexico, and his PhD in optics in 1999 from the National Institute of Astrophysics, Optics, and Electronics, where he is now an associate researcher in the Optics Department. His research interests include optical information processing, optical-digital systems, and mathematical morphology.

Fermín Granados-Agustín is a researcher with the Optics Department of the National Institute of Astrophysics, Optics, and Electronics (INAOE), Mexico. He received his BS degree in physics from the National University of Mexico (UNAM) in 1993. He received his MS degree and PhD degree in optics, respectively in 1995 and 1998, both from the INAOE. He is a national researcher for the National System of Researches, Mexico. He held a postdoctoral position at the Mirror Lab of the Steward Observatory at the University of Arizona in 1999. He has been the head of the optical shop at INAOE since 2005. His research interests include optical information, interferometric optical testing, and instrumentation.

Alejandro Cornejo-Rodríguez received his physics degree in 1964 from the Mexican National Autonomous University, his MS degree in optics in 1968 from Rochester University, and his PhD in optics in 1982 from Tokyo Institute of Technology, Japan. He is now a senior researcher in the Optics Department at the National Institute of Astrophysics, Optics, and Electronics. His research interests include optical metrology, optical surface testing, and optical image processing.